Organic Modulators Enable Morphological Diversity in Colloidal Crystals Engineered with DNA

Nikhil S. Chellam[1,2,‡], *Heather A. Calcaterra*[1,2,‡], *Qinsi Xiong*[2,3,‡], *George C. Schatz*[1,2,3,*], and *Chad A. Mirkin*[1,2,3,*]

‡These authors contributed equally to this work.

*Corresponding authors: g-schatz@northwestern.edu, chadnano@northwestern.edu

[1]Department of Chemical and Biological Engineering, Northwestern University, Evanston, IL, 60208, United States

[2]International Institute for Nanotechnology, Northwestern University, Evanston, Illinois 60208, United States

[3]Department of Chemistry, Northwestern University, Evanston, IL, 60208, United States

ABSTRACT

Colloidal crystal engineering with DNA is a powerful way of generating a wide variety of crystals spanning over 90 different symmetries. However, in many cases, crystals with well-defined habits are difficult, if not impossible, to make, in part due to rapid crystal defect formation and propagation. This is especially true in the case of face-centered cubic (FCC) structures. Herein, we report a strategy that uses formamide as a chemical modulator to slow down colloidal crystal growth, which decreases defect formation and yields higher-quality crystals. Formamide forms hydrogen bonds with DNA bases and destabilizes the DNA duplex; in the context of colloidal crystallization, formamide leads to the disassembly of undercoordinated particles (defect architectures) and facilitates their reassembly into structures with the maximum number of nearest-neighbor contacts and DNA bonds. When targeting an FCC lattice comprised of DNA-modified spherical 20 nm particles, formamide promotes the formation of its Wulff polyhedron (a truncated octahedron), never observed before in colloidal crystal engineering with DNA. Importantly, kinetic habits, including octahedra, icosahedra, and decahedra, are also observed depending on formamide concentration.

KEYWORDS: Gold, Crystallization, X-ray scattering, Directed self-assembly, Nucleic acids

TOC GRAPHIC

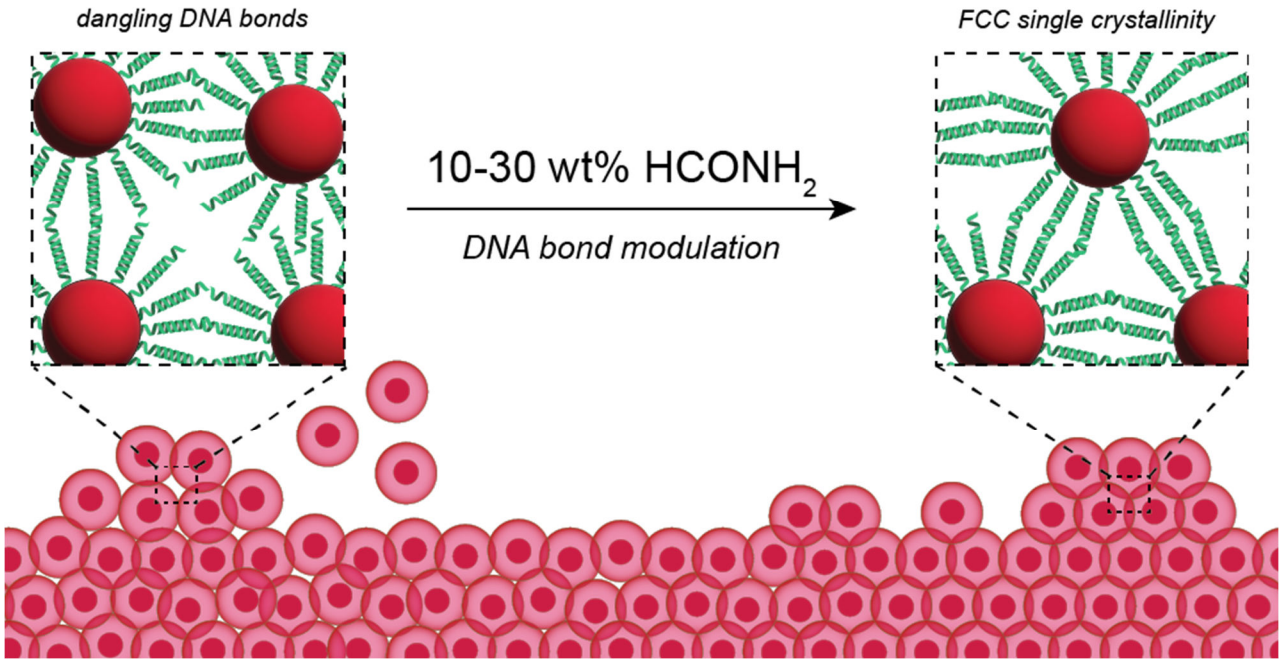
dangling DNA bonds
FCC single crystallinity
10-30 wt% HCONH2
DNA bond modulation

Due to their tunable chemical composition and duplex formation characteristics that are sensitive to their dielectric environment, nucleic acids are powerful programmable, stimuli-responsive surface ligands that can be used to direct the assembly of nanoparticles into well-defined colloidal crystals (CCs).[1, 2] Within this framework, colloidal nanoparticles ("atoms") coated with a dense shell of oligonucleotides (programmable "bonding elements") function as "programmable atom equivalents" (PAEs). Hybridization events between adjacent PAEs induce "bond formation" and crystallization.[3] By changing the oligonucleotide sequence and particle types, superlattices can be realized that span over 90 different symmetries and multiple crystal habits.[4-8] Particle spacing can be controlled over the 5-100 nm length scale with sub-nm precision.[9-11] Furthermore, since these programmable interactions or bonding characteristics are independent of the particle core (a key difference when compared to traditional atoms), different core compositions can be employed to realize structures with unusual photonic, catalytic, and mechanical properties.[12-16]

While in certain cases, it is possible to obtain DNA-engineered crystals with well-defined habits and, in fact, ones that are the thermodynamic Wulff construction,[5, 6, 17] in many others it has been difficult or thus far impossible *via* solution-phase slow cooling approaches.[18-20] The face-centered cubic (FCC) structure is a prime example. While polycrystalline forms have been known since the seminal days of colloidal crystal engineering with DNA,[3, 6, 21-27] no one has prepared it in single crystal form and in particular realized the truncated octahedral Wulff polyhedron, which comprises eight (111) and six (100) facets.[28-31] This is presumably due to competition with the kinetic HCP phase,[32] as well as a similarity in surface energies for its exposed facets.[19, 33, 34] This lowers the energy barrier for crystal defects, including stacking faults and twinning, thereby resulting in different (or undefined) habits and/or amorphous aggregates.

In this regard, we hypothesized that a DNA denaturing agent such as formamide could be used as a modulator[35] to slow down crystal growth and realize higher-quality macroscopic crystals. Formamide's ability to interfere with DNA base pairing (by competing with hydrogen bonding sites) has often been used in the context of DNA origami to realize higher-quality architectures.[36-38] Herein we show that under the appropriate conditions it can also be used in the context of colloidal crystal engineering with DNA to dramatically increase crystal quality and, even in the case of an FCC structure, realize the truncated octahedral Wulff construction. By studying its role both experimentally and through molecular dynamics (MD) simulations, we have devised a strategy to realize kinetic habits as well.

RESULTS AND DISCUSSION

To test this hypothesis, we formed FCC-structured CCs with 20-nm spherical Au particles and a self-complementary DNA linker sequence **(Table S1)** with formamide concentrations (C_F; measured in wt%) ranging from 0 to 30%. Scanning electron microscopy images show that increasing C_F (below a threshold value of 20%) yields FCC single crystals. These structures have similar morphologies to those previously observed *via* slow-drying[16, 31] and covalent linkages[30, 39, 40] to drive colloidal crystallization (additional images are provided in the **Supporting Information**). At 0%, we observed agglomerated CCs with irregular habits, while maintaining FCC crystallinity, as evidenced by FCC{111} surface planes **(Figs. 1a, S1)**. However, at 15-20%, a diverse array of tetrahedral, octahedral and hexagonal CCs was observed with varying degrees of truncation **(Figs. 1b, 1d)**. These superlattices possess a mixture of (111) and (100) facets indicating a tendency towards the FCC Wulff constructions for single and planar-twinned crystals **(Figs. 1ci-ii, S2-S4)**.[41] The presence of truncated tetrahedra (a lower symmetry T_d product compared to the O_h symmetries usually observed for FCC crystals) is rather unusual, suggesting

kinetic control over the formation of these colloidal single crystals.[31, 42, 43] However, while octahedral CCs solely possessing (111) facets, fivefold twinned decahedra, and 20-fold twinned icosahedra (i.e., kinetic products) are occasionally observed at 30%, other irregularly-shaped byproducts predominate **(Fig. 1e-f, S5-S6)**.

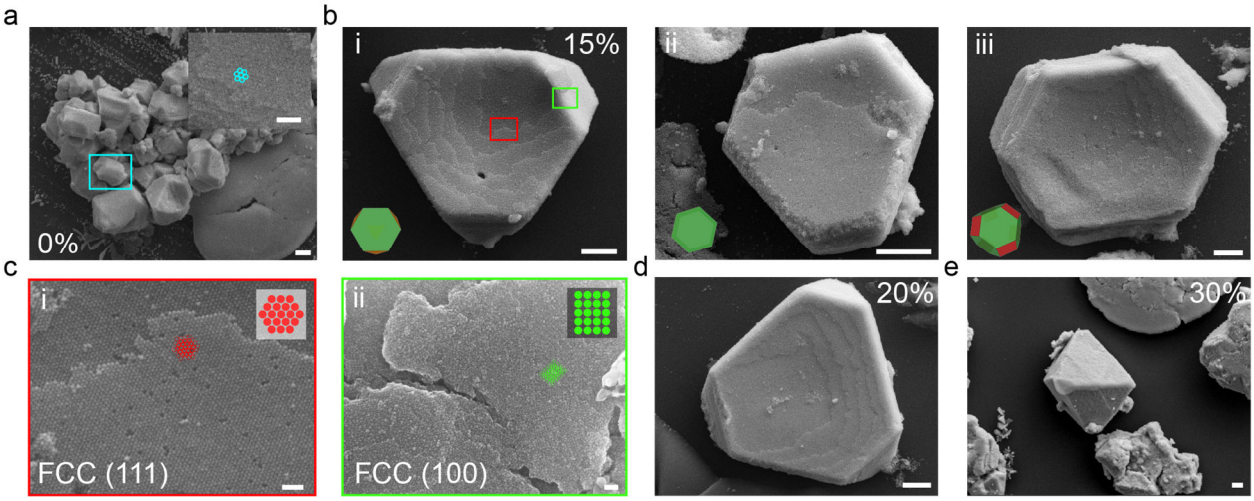

Figure 1: Scanning electron microscopy images of FCC-structured colloidal crystals with C_F. **(a)** C_F = 0%, scale bar = 1 µm. The inset indicates surface FCC crystallinity, with overlay showing FCC(111) configuration. **(b)** A variety of **(i)** truncated tetrahedral (kinetic, single-crystalline Wulff polyhedron) **(ii)** truncated triangular (kinetic, planar-twinned Wulff polyhedron), and **(iii)** truncated octahedral (thermodynamic Wulff polyhedron) structures with C_F = 15%. Scale bar = 1 µm. **(c)** Zoomed-in and tilt images of (3b-i) in the regions demarcated by colored boxes, revealing **(i)** FCC(111) and **(ii)** FCC(100) planes, respectively. Crystal stacking is shown in the inset. Scale bars are 100 nm. **(d)** Truncated tetrahedron with C_F = 20% and **(e)** representative octahedral CC with C_F = 30 %; scale bars = 1 µm.

Interestingly, these crystals exhibit layer-by-layer terracing **(Fig. 1c, S2d)**. In atomic crystallization, terraces form when fluctuations in temperature or supersaturation lead to uneven layering as the crystal grows.[44-46] In a previous study, we hypothesized that colloidal crystallization initiates from the living polymerization and rearrangement of aggregated clusters to form larger microcrystals.[47] These observations indicate that formamide could promote the reversible hybridization of aggregated clusters on the CC surface. Any steps on the edges of such terraces should serve as sites for further growth.[30, 44, 48] Moreover, in our experiments, the CCs qualitatively

exhibit less (111) truncation than in those predicted from previously reported surface enthalpy calculations, which, together, suggests the significant role of surface entropy in this particular system.[19]

From these observations, we hypothesized that formamide slows down the rate of CC formation, thereby leading to faceted architectures. To study the kinetics of PAE hybridization in these mixed organic-aqueous solutions, we obtained melting hysteresis curves in solutions of varying C_F **(Fig. 2a**). The denaturation temperature (T_D) reflects the stability of the DNA duplex, while the renaturation rate provides insight into the DNA rehybridization kinetics as the temperature is slowly cooled.[49, 50] From these melting curves, as C_F increases, we observe a monotonic decrease in melting temperature, with the renaturation temperature (T_R) going below room temperature at 30% formamide. This trend agrees with prior reports for free DNA, where melting temperatures are observed to decrease by ~0.6 ºC per wt% formamide.[51, 52]

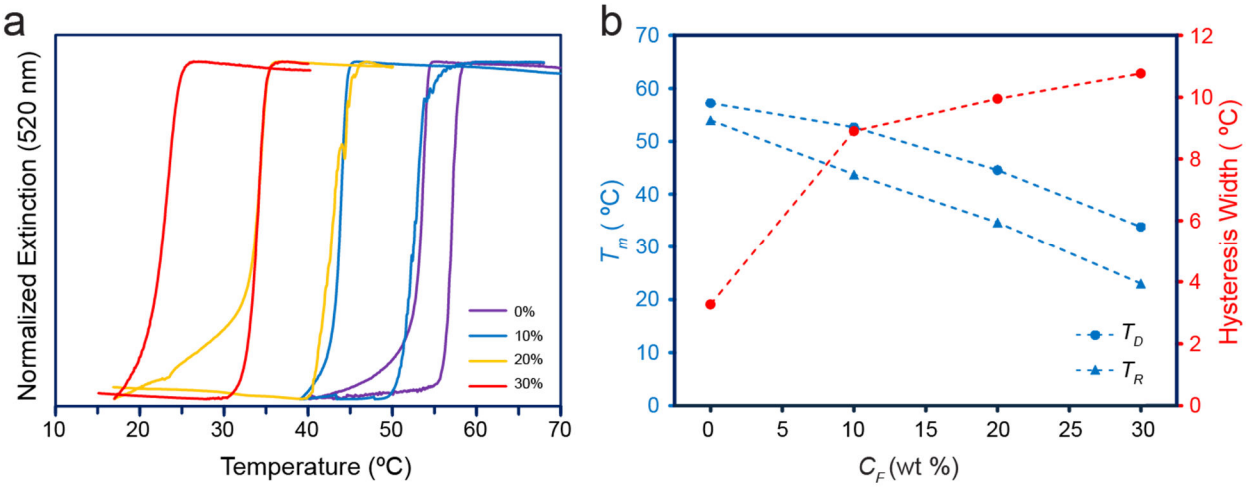

Figure 2. Hybridization thermodynamics of 20 nm PAEs with varying C_F. **(a)** Normalized UV-vis PAE melting curves and **(b)** corresponding denaturation and renaturation temperatures (T_D and T_R), alongside hysteresis width.

Notably, as C_F increases, the hysteresis width concomitantly broadens **(Fig. 2b)**. This effect is more pronounced at lower C_F, where the width broadens by nearly 6 ºC between 0 and 10%.

However, increasing formamide content beyond 10% has diminishing contributions towards this broadening. A wider hysteresis implies a greater disparity between the conditions required for PAE denaturation and renaturation (i.e., thermodynamic irreversibility), as the denatured, single-stranded DNA is now thermodynamically stabilized.[49, 50, 53, 54] As increasing C_F leads to a wider hysteresis, we hypothesize that formamide promotes lattice reorganization as the CC grows when cooled, thereby yielding FCC single crystals. Analogous processes include oxidative etching in canonical NP syntheses and coordination modulation in the metal-organic framework realm, whereby kinetically-trapped dangling bonds between building blocks are readjusted through iterative dissolution and reprecipitation, leading to faceted, single-crystalline architectures.[55-57] Indeed, a similar dynamic modulation approach has been demonstrated through the use of oligoanions to electrostatically modulate colloidal crystallinity in Au nanoparticle superlattices.[58] While formamide denaturation has been widely studied for their linear, free counterparts, the collective nature of DNA hybridization in PAEs renders this system prone to kinetic traps, wherein each PAE does not maximize the number of hybridization events with its nearest neighbors.[59, 60] In these dynamically arrested states, the PAE cannot disassemble and settle into its closest-packed configuration.[61-63] In contrast, these data suggest that denaturation events could thermodynamically control PAE hybridization by prolonging duplex renaturation at low temperatures. Supporting this mechanistic picture, we find that increasing C_F both slows the renaturation rate and increases its full width-half maximum (FWHM; **Fig. S5**). This extended renaturation transition, then, confers more time for each PAE to equilibrate into its minimum energy configuration, thus promoting the formation of well-ordered structures.

The thermodynamics of surface-immobilized DNA markedly differs from that of free DNA in solution, primarily due to constraints on its conformational degrees of freedom – a phenomenon

common to all surface-tethered polymers.[64-66] Consequently, to gain a molecular-level insight into formamide effects on PAE binding, a series of all-atom MD simulations were performed. Computational scalability limits the extent to which a full PAE can be simulated for such all-atom calculations; thus, this model involved four DNA strands tethered onto two 24 nm^2 planar surfaces (a grafting density consistent with previous reports[6, 67]) with identical sequences to those used experimentally. Analysis of a 2D contact map of these Au-tethered DNA strands indicates that the base pair contact number decreased with increasing formamide content **(Figs. 3a, S7)**. At 30% formamide, the number of base pair contacts neighboring the flexible hexa(ethylene glycol) spacer is lower than those under purely aqueous conditions **(Fig. 3a)**. This observation suggests that duplex denaturation by formamide originates and propagates ("unzips") adjacent to the particle surface and the sticky ends governing contacts between PAEs.

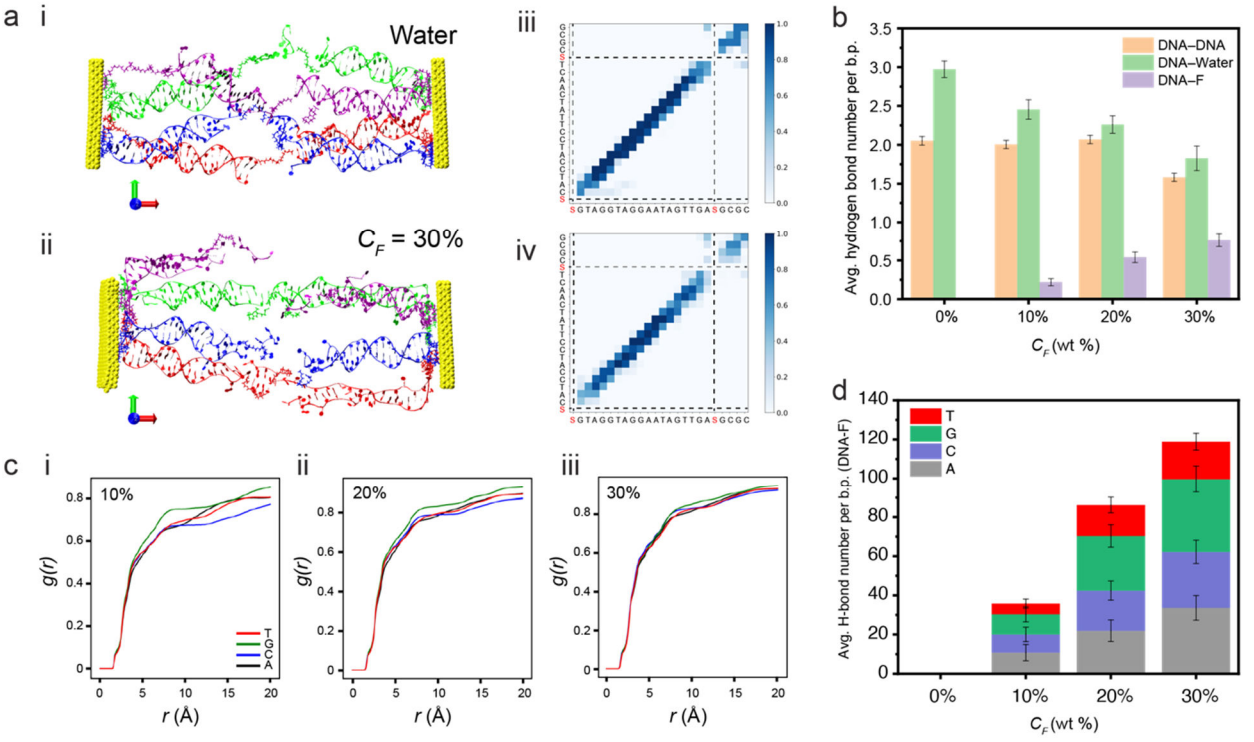

Figure 3. Molecular dynamics simulations of Au-tethered DNA with the formamide weight percentage (C_F) listed. **(a)** Representative snapshots of **(i)** water and **(ii)** formamide Au NP/DNA configurations after a 300 ns trajectory, and 2D contact maps for **(iii)** water and **(iv)** 30 wt%

formamide. Interstrand base pairs form a contact if their interatomic separation is shorter than 0.45 nm. Dashed lines indicate the hexa(ethylene glycol) spacer *S*. **(b)** Average hydrogen bond number per base pair between base pairs, base pairs and water, and base pairs and formamide (F). A pair of N/O–H···O=C (or N/O) groups is considered to form a hydrogen bond if the distance between donor and acceptor atoms is less than 0.35 nm and the donor-acceptor angle is greater than 120º. **(c)** Radial distribution function *g(r)* of formamide-base pairs per C_F. **(d)** Average formamide-base pair hydrogen bond number per C_F, broken down by base.

Further examination of the average number of hydrogen bonds per base pair **(Fig. 3b)** shows that while bonds between base pairs remain invariant between C_F = 0 to 20%, the number of DNA bonds with formamide increases at the expense of those with water. This indicates that at reduced C_F, formamide preferentially displaces water from the DNA solvation shell while minimally, if not transiently, interfering with base pairing. While formamide and water can both form three hydrogen bond contacts, nucleic acid hydration is necessary to maintain DNA's double helix; formamide destabilizes DNA duplexes by displacing loosely bound water molecules.[68, 69] However, at 30%, the number of hydrogen bonds between base pairs begins to decrease, showing that above a threshold concentration, formamide non-selectively displaces not only water-DNA hydrogen bonds but also those between DNA bases.

Formamide is known to preferentially interact with GC-rich regions in the DNA strand, as AT-specific regions have tightly-bound immobilized water bridges that support the helix within the minor groove.[51] This is further shown in the radial distribution function, where, at low C_F, formamide concentrates mostly in G-rich regions as both can form three hydrogen bonds **(Fig. 3c)**. Nevertheless, this GC-selectivity diminishes at elevated C_F, where each base has a roughly equal chance of formamide coordination above 20% **(Figs. 3cii-iii, 3d)**. Furthermore, Eichinger and Fixman hypothesize that an increase in hysteresis width can be attributed to increased conformational entropy (in this case, induced by favorable DNA-formamide interactions) and a resultant heterogeneity in interstrand correlations.[53, 70] This rationale concurs with the increase in

DNA-formamide hydrogen bond number at the expense of those between base pairs **(Fig. 3b)** and the large increase in hysteresis width with C_F (*vide supra;* **Fig. 2b**).

Superlattices in each case show well-resolved small-angle X-ray reflections characteristic of FCC ordering **(Fig. 4a)**. Increasing C_F shows slight, though non-monotonic, shifts to higher scattering wavevectors in the first peak position (q_0), suggesting negligible changes in lattice parameter with C_F **(Table S3; Supplementary Text)**. Moreover, analysis of peak width in SAXS spectra gives insight into lattice strain as well as CC size and polydispersity.[71-73] Initially, the SAXS data show a FWHM narrowing from 0 to 15% C_F, indicating a decrease in diffuse scattering events concomitant with increasing crystallite homogeneity **(Fig. 4b)**. However, if too much formamide is added, DNA binding between PAEs is weakened to the extent that long-range ordering is inhibited. Indeed, the SAXS FWHM broadens beyond 15% to greater than 0.015 Å^{-1} at 30%, suggesting a combination of increased crystallite strain arising from defect formation concurrent with decreasing (111) domain size.

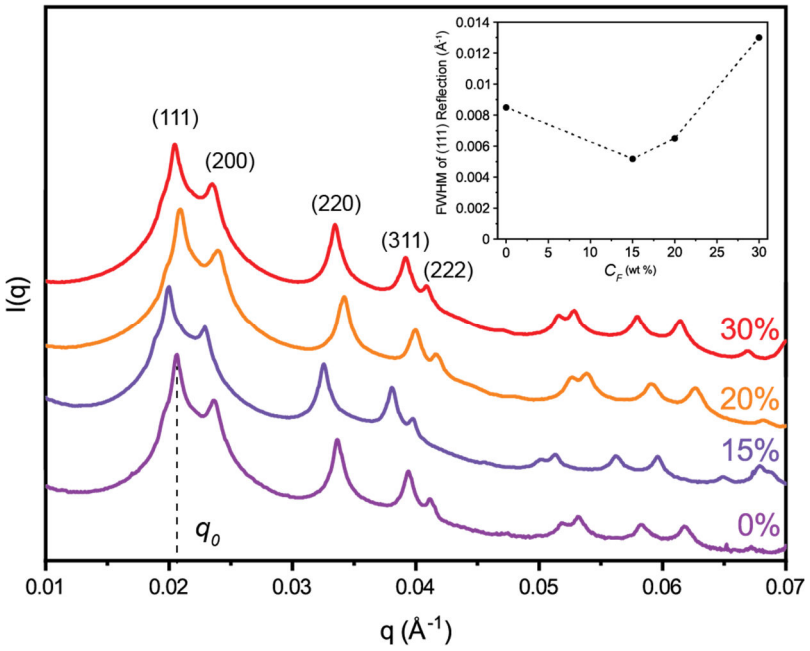

Figure 4: SAXS spectra of CCs synthesized with increasing C_F (0 to 30%) and indexed reflection planes. The inset shows the FWHM associated with the (111) reflection (at q_0) per C_F.

CONCLUSIONS

Taken together, relative CC homogeneity occurs at moderate (i.e., 10-20%) C_F. Formamide, then, provides another handle to modulate the DNA interaction strength and barriers to PAE reorganization within a lattice. However, if T_R is too low, then even cooling to room temperature is insufficient to form ordered structures, leading to kinetically arrested states without distinct faceting. Indeed, assembly processes can generally be seen as a tradeoff between thermodynamic and kinetic driving forces. As the system is cooled below a characteristic kinetic crossover temperature, the equilibrium ordered state becomes increasingly probable, though at the expense of the assembly rate.[74-77] Formamide can then be understood to modulate both T_R and the kinetic crossover temperature. Thus, while increasing C_F to 30% (where T_R is approximately room temperature) enables occasional octahedral, decahedral, and icosahedral habits, the binding between particles is too weak to lead to stable structures on average, resulting in increased polydispersity and irregularities in crystal habit.

This work shows that molecular additives can be used as kinetic control elements to guide colloidal crystal assembly with DNA. Consistent with some of the conclusions drawn herein, Macfarlane and coworkers recently reported using formamide to increase the size of colloidal crystals in the context of BCC structures.[78] Herein, we demonstrate it to be an effective strategy to form difficult-to-realize crystal habits (due to surface and stacking energy similarities) and promote long-range crystallinity. Moreover, we show that an optimum C_F is essential for maximizing these effects; too much formamide weakens the DNA bond strength to the point that ordered structures do not form. Therefore, this should not be confused with post-synthetic "stapling strategies" which increase bond strength following crystal formation.[79-81] Finally, this

modulator strategy not only provides a route towards engineering crystal habit but also more generally extends our understanding of nanoparticle systems as models of atomic materials.

METHODS

All precursors were purchased from Sigma-Aldrich and used without further purification unless otherwise stated. Spherical, cetylpyridinium-stabilized 20 nm gold nanoparticles were synthesized via an iterative growth/dissolution process as previously reported.[55] These particles were then centrifuged twice (3180 rpm) and redispersed in 0.1 M trisodium citrate prior to DNA functionalization. Alternatively, 20 nm spherical gold nanoparticles were purchased from Ted Pella. To inhibit interference of decarbonylative products (i.e. carbon monoxide and ammonia), deionized formamide solutions were sparged with N_2 for at least 30 minutes prior to usage **(Figure S13)**. Detailed synthetic protocols and analytical procedures are discussed in the **Supporting Information**.

DNA Synthesis and Purification

Gold nanoparticles were functionalized with a single-stranded 3′-thiol-modified "anchor" sequence. A second self-complementary "linker" strand was then hybridized to each anchor strand, causing aggregation of the particles. Oligonucleotides were synthesized on an automated MerMade 12 synthesizer with phosphoramidites purchased from Glen Research. The DNA design used in this work was taken from the literature **(Table S1)**.[19]

Structure	Description	DNA Sequence (5′ to 3′)
Face-centered Cubic (FCC)	Anchor DNA	TCA ACT ATT CCT ACC TAC $(Sp18)_2$ SH
	Self-complementary linker DNA	GTA GGT AGG AAT AGT TGA (Sp18) GCGC

Table 1. DNA sequences used in this work.

Controlled pore-glass (CPG) beads with a 3' propylthiol group were used to synthesize "anchor" DNA strands for Au nanoparticle functionalization. Universal CPG beads were used to synthesize linker DNA sequences. After cleavage from the CPG support *via* immersion in 30% v/v aqueous ammonia, strands bearing a 5' dimethoxytrityl (DMT) group were purified via reverse-phase high-performance liquid chromatography (HPLC; Agilent), on a C18 column with 0.03 M triethylammonium acetate at pH 7 and a 1% per minute gradient prior to removal of the DMT group in acid. Matrix-assisted laser desorption ionization time-of-flight mass spectrometry (MALDI-ToF-MS) was used to confirm the molecular weight of the HPLC-purified oligonucleotides. The OligoAnalyzer tool from Integrated DNA Technologies was used to determine the extinction coefficient of each DNA strand (available free of charge at https://www.idtdna.com/pages/tools/oligoanalyzer), and UV-vis spectroscopy was used to determine DNA concentrations.

Nanoparticle Functionalization with DNA

Spherical gold nanoparticles were functionalized with 3′ thiolated oligonucleotides to form programmable atom equivalents (PAEs), as previously reported.[3, 19] Briefly, thiolated oligonucleotides were treated with either a 100 mM solution of dithiothreitol (DTT) in 170 mM sodium phosphate buffer (pH = 7.4) for 1 h, or 50 mM tris(carboxyethyl)phosphine hydrochloride (TCEP-HCl) in neutral DI water. Residual DTT or TCEP-HCl was removed using NAP-5 size exclusion columns (GE Healthcare). Concurrently, 1 mL of the nanoparticles (~1 OD) were centrifuged at 3200 rpm, the supernatant was removed, and the particles were resuspended in fresh deionized water. The particles were centrifuged a second time at 3180 rpm, the supernatant was removed, and the DNA was added directly to the pellet of nanoparticles (1 OD of DNA was added per mL of nanoparticle solution). Sodium phosphate buffer (1 M, pH = 7.4) and 1 wt% sodium

dodecyl sulfate (SDS) were added to the nanoparticle solution to make the concentration 0.1 M and 0.01 wt% respectively, the solutions were briefly sonicated and then placed on a shaker for 2 h. After this, 2 M NaCl (aq) was added to the nanoparticle solutions every half hour such that the final concentration of each solution was 0.05, 0.1, 0.2, 0.3, 0.4, and 0.5 M NaCl after each successive addition. The nanoparticle solutions were briefly sonicated after each addition. Following the last NaCl addition, the nanoparticles were placed on a shaker at 1,000 rpm for at least 12 h to ensure a dense loading of oligonucleotides. After this time, each nanoparticle solution was centrifuged three times to remove excess DNA, with the supernatant removed each time and replaced with a solution of 0.5 M NaCl, 0.01 M sodium phosphate buffer (pH = 7.4), and 0.01 wt % SDS.

Nanoparticle Assembly with DNA

A stock solution was prepared by combining concentrated PAEs with the self-complementary linker and PBS buffer containing 0.5 M NaCl and 0.01% SDS (to prevent heterogeneous nucleation) in a 200 µL PCR tube. The final concentration of nanoparticles and linker strands were 10 OD and 40 OD, respectively, in a total volume of 100 µL. Upon addition of the self-complementary linker, the solution changed from red to purple to grey, indicating nanoparticle aggregation. Next, varying amounts of formamide (0 wt%, 15 wt%, 20 wt% and 30 wt%) were added such that the total volume of each sample remained at 100 µL. To grow the colloidal crystals, the aggregated NPs were heated to 68 ºC using a Veriti Thermal Cycler 96-well instrument (Life Technologies), under which conditions the solution changed back to red, indicating full dispersion and melting of the aggregates. The solution was left to cool at a rate of 0.1 ºC/10 min to 24 ºC to promote superlattice formation. We additionally attempted to grow

faceted FCC single crystals using a slower cooling rate of 0.1 ºC/20 min at 0% C_F, though no faceted FCC single crystals were observed (**Figure S14**).

Silver Embedding of CCs

Nanoparticle superlattices were transferred to the solid state *via* Ag^+ ion intercalation according to a previously-reported method.[82] Briefly, the SLs were transferred to a 1.5-mL Eppendorf tube containing 1 mL of fresh 0.5 M $NaClO_4$ containing 0.01 wt% sodium dodecyl sulfate, allowing for the crystals to sediment at the bottom of the tube. This procedure was repeated three times with a 15-minute interval between each washing step, after which the particulates were then transferred into a solution containing 1 mL of 0.5 M aqueous $AgNO_3$, and the mixture was left to incubate overnight. The sample was then washed 3x with fresh deionized water, and then 2 µL of solution containing the assemblies was drop cast on a silicon wafer for subsequent imaging.

Scanning Electron Microscopy Characterization

SEM images of nanoparticle superlattices were taken with a JEOL JSM-7900 field emission SEM with a 15 kV acceleration voltage and a current of 20 µA.

Small-angle X-ray Scattering Measurements

Small-angle X-ray scattering experiments were carried out at Sector 5 of the Advanced Photon Source at Argonne National Laboratory in the DuPont-Northwestern-Dow Collaborative Access Team (DND-CAT) beamline. An X-ray wavelength of 1.23 Å (10 keV) was used for experiments, and the detector was calibrated using silver behenate and a silicon diffraction grating sample. Two sets of slits were used to collimate and define the beam. Approximately 40 µL of each sample was aliquoted into 1.5 mm Charles Supper quartz capillary tubes. Typical exposure times for the experiments ranged from 0.1 to 0.5 s. Scattered radiation was measured using a CCD

detector. 2D diffraction data was azimuthally averaged to generate a 1D SAXS data plot with scattering intensity I(q) as a function of the scattering parameter q, where q is:

$$q = \frac{4\pi \sin(\theta)}{\lambda};$$

in this equation, λ is the wavelength of the X-ray radiation and θ is the scattering angle.

The scattering measurement includes the buffer, DNA, structure factor, form factor, and the capillary tubes. The structure factor was determined using the relationship

$$I(q) = \frac{S(q)}{F(q)},$$

where *I(q)* is the measured scattering intensity, *S(q)* is the structure factor arising from colloidal ordering, and *F(q)* is the form factor intrinsic to the individually dispersed particles. The form factor can either be simulated or experimentally determined for a suspension of free particles (as was done in this work).[72, 83]

The nearest neighbor distance *d* (in nm) between particles in an FCC superlattice can be calculated from the position of the first scattering peak q_0 in a SAXS spectrum from

$$d = \frac{\pi\sqrt{6}}{10\, q_0}.$$

Once this nearest neighbor distance is calculated, the lattice parameter *a* can be determined from a trigonometric relationship for the FCC unit cell; that is,

$$a = d\sqrt{2}.$$

The relationship between grain size and peak width is governed by the Scherrer equation, or

$$\xi_{hkl} = \frac{K\lambda}{\beta_{hkl}\cos(\theta_{hkl})} = \frac{2\pi K}{\Delta q_{hkl}}.$$

In this equation, ξ_{hkl} is the orientational correlation length for the crystal plane of interest, over which the lattice directionality is roughly preserved, λ is the X-ray wavelength (1.23 Å), β_{hkl} is the peak width (FWHM) associated with a particular reflection, and θ_{hkl} is the corresponding scattering angle. The shape factor K takes on different values depending on the grain shape, grain size distribution and how the peak width is defined. For the spherical particles used in this work, we define it as $K = 2\sqrt{\frac{\ln(2)}{\pi}} \approx 0.9$.[84]

To determine these values, the structure factor S(q) was fit to a Pearson type VII function, such that

$$S(q) = \sum_{q} M * \left[1 + \frac{(\mathrm{q} - \mu)^2}{ma^2}\right]^{-m},$$

where M is the peak height, μ is the peak center, a is proportional to the peak full width at half maximum (FWHM), and m denotes the rate at which the tail of the peak profile falls. Simulated curves were generated using the Irena extension to Igor Pro (available free of charge at https://usaxs.xray.aps.anl.gov/software/irena).[85] These simulated patterns were then compared to experimental curves to determine lattice parameters and symmetries.

UV-vis melt experiments

UV-vis melt experiments were carried out at different conditions using an Agilent Cary 5000 UV-vis spectrophotometer. To measure the melting transitions, 1 OD of PAEs and 4 OD of linker were diluted to 1 mL of 1 OD nanoparticle solution using water (912 µL, 823 µL, and 735 µL), formamide (88 µL, 177 µL, and 265 µL), and NaCl such that the total salt concentration

added to 0.5 M NaCl. Samples were then placed in cuvettes with magnetic stir bars. The extinction of the solution was monitored at 520 nm near the excitation wavelength of the plasmonic nanoparticles. For melt experiments, the samples were heated from 15 °C to 70 °C at a rate of 0.1 °C/min, and then cooled back down to 15 °C at the same rate.

Molecular Dynamics Simulations

All-atom MD simulations were performed to study the interactions between formamide/water mixtures and Au-tethered self-complementary DNA strands. Here, we modeled a small section of the two gold nanoparticle surfaces connected by 4 single strands of B-type DNA (each DNA linker consists of two double-stranded fragments that are connected by sticky ends; see **Figure S8**). We used identical DNA sequences (**Table 1**) to those used in our experiments. The initial helical parameters of the ds-DNAs are adapted from the canonical B-DNA structure and are built using web 3DNA.[86] To model the PAE surfaces, we used Avogadro[87] to build two flat Au(111) slabs with dimensions of 55.05 Å × 55.05 Å × 4.08 Å. The distance between the DNA axes is taken to be 28.5 Å, which is comparable to the experimental value for small (∼10 nm) gold particles.[67] Each DNA strand was attached to a single gold surface atom using a thiol-$(sp18)_2$ anchor. Parameters were taken from Heinz et al. for the gold surface.[88] We used the CHARMM36 force field for DNA[89] and CHARMM general force field for formamide and thiol-$(sp18)_2$.[90] The two Au surfaces with 4 DNA strands were placed in a rectangular box of size 60 Å × 60 Å × 230 Å and solvated with 100% TIP3P water or a mixture of 90% to 70% TIP3P and 10% to 30% formamide, respectively (see **Table 2** for the number of water and formamide molecules added in each system). We additionally performed simulations using 80% formamide to compare against previous observations made using low-dielectric solvents **(*c.f.* Supplementary Text)** We reserved a 5 Å gap between the unfunctionalized gold surfaces (i.e., between their periodic images) to allow

the free passage of solvents and ions. 308 Na^+ ions were added to neutralize the system. For each simulation, we also added 249 Na+ and 249 Cl^- ions for consistency with the 0.5 M salt concentrations used experimentally.

C_F	0%	10%	20%	30%
N_{H2O}	22158	19942	17726	15511
N_F	0	1001	2001	3002

Table 2. Number of water (N_{H2O}) and formamide (N_F) molecules added to the simulations per C_F.

We used NAMD *v.* 2.13 to perform our all-atom MD simulations.[91] All systems were subject to a 15000 step energy minimization scheme followed by a 1 ns NVT ensemble with both the gold surface and DNA positionally constrained at 300K using the Langevin piston as implemented in NAMD.[92] Afterwards, we slowly relaxed the constraints and conducted another 5 ns simulation using the NPT ensemble at 300K and 1 atm using the Langevin piston[92] and the Nose-Hoover method[93] as implemented in NAMD. The temperature was maintained with a damping coefficient of 5 ps^{-1} using Langevin dynamics while the pressure was kept at 1 atm with a Langevin piston period of 400 fs and a damping time constant of 200 fs. The particle mesh Ewald method[94] was employed to calculate electrostatic interactions with a short-range cutoff of 1.2 nm. Periodic boundary conditions were employed with a simulation time step of 2 fs using the SHAKE algorithm. Each production run consisted of a 300 ns simulation using the NVT ensemble.

ASSOCIATED CONTENT

Supporting Information

DNA sequences, additional methods and materials, molecular dynamics data, DNA melting, additional low- and high-magnification SEM images of colloidal crystals per C_F, and additional discussion comparing formamide denaturation with low-dielectric solvents. (PDF)

AUTHOR INFORMATION

Corresponding Authors

*g-schatz@northwestern.edu

*chadnano@northwestern.edu

Author Contributions

‡ N.S.C., H.A.C., and Q.X. contributed equally to this work. Conceptualization: N.S.C., H.A.C., G.C.S., and C.A.M.; Methodology: N.S.C., H.A.C., and Q.X.; Investigation and Formal Analysis: H.A.C., N.S.C., Q.X., G.C.S., and C.A.M.; Writing – Original Draft: N.S.C.; Writing – Review & Editing: N.S.C., C.A.M., G.C.S., Q.X., and H.A.C.; Supervision: G.C.S. and C.A.M. All authors were involved in the writing and data analysis process and have approved the final version of the manuscript.

Funding Sources

N.S.C., H.A.C., and C.A.M. acknowledge support from the Air Force Office of Scientific Research award FA9550-22-1-0300 (electron microscopy, small-angle X-ray scattering, and materials synthesis). N.S.C., H.A.C, Q.X., C.A.M, and G.C.S. additionally acknowledge support from the Center for Bio-Inspired Energy Science, an Energy Frontier Research Center funded by the U.S.

Department of Energy, Office of Science, Basic Energy Sciences award DE-SC0000989 (theoretical modeling, electron microscopy, materials synthesis). N.S.C. and H.A.C. acknowledge support from the National Science Foundation Graduate Research Fellowship through grants DGE-2234667 and DGE-1842165, respectively. Any opinions, findings, and conclusions, or recommendations expressed in this material are those of the authors and do not necessarily reflect the views of the National Science Foundation. This work made use of Northwestern University's NUANCE Center, which has received support from the SHyNE Resource (NSF-ECCS-2025633), the International Institute for Nanotechnology, and the Northwestern University Materials Research Science and Engineering Center (NSF DMR-2308691).

ACKNOWLEDGMENT

N.S.C. is grateful to Drs. Noel J. Leon and Sarah H. Petrosko for editorial input.

ABBREVIATIONS

CC, colloidal crystal; PAE, programmable atom equivalent; FCC, face-centered cubic; HCP, hexagonal close-packed; MD, molecular dynamics; C_F, formamide concentration (in wt%); T_m, DNA melting temperature; T_D, DNA denaturation temperature, T_R, DNA renaturation temperature; FWHM, full width-half maximum; SAXS, small-angle X-ray scattering.

REFERENCES

(1) Mirkin, C. A.; Letsinger, R. L.; Mucic, R. C.; Storhoff, J. J. A DNA-based method for rationally assembling nanoparticles into macroscopic materials. *Nature* **1996**, *382* (6592), 607-609. DOI: 10.1038/382607a0.

(2) Mirkin, C. A.; Petrosko, S. H. Inspired Beyond Nature: Three Decades of Spherical Nucleic Acids and Colloidal Crystal Engineering with DNA. *ACS Nano* **2023**, *17* (17), 16291-16307. DOI: 10.1021/acsnano.3c06564.

(3) Park, S. Y.; Lytton-Jean, A. K. R.; Lee, B.; Weigand, S.; Schatz, G. C.; Mirkin, C. A. DNA-programmable nanoparticle crystallization. *Nature* **2008**, *451* (7178), 553-556. DOI: 10.1038/nature06508.

(4) Macfarlane, R. J.; Lee, B.; Jones, M. R.; Harris, N.; Schatz, G. C.; Mirkin, C. A. Nanoparticle Superlattice Engineering with DNA. *Science* **2011**, *334* (6053), 204-208. DOI: doi:10.1126/science.1210493.

(5) O'Brien, M. N.; Lin, H.-X.; Girard, M.; Olvera de la Cruz, M.; Mirkin, C. A. Programming Colloidal Crystal Habit with Anisotropic Nanoparticle Building Blocks and DNA Bonds. *Journal of the American Chemical Society* **2016**, *138* (44), 14562-14565. DOI: 10.1021/jacs.6b09704.

(6) Laramy, C. R.; O'Brien, M. N.; Mirkin, C. A. Crystal engineering with DNA. *Nature Reviews Materials* **2019**, *4* (3), 201-224. DOI: 10.1038/s41578-019-0087-2.

(7) Kim, Y.; Macfarlane, R. J.; Jones, M. R.; Mirkin, C. A. Transmutable nanoparticles with reconfigurable surface ligands. *Science* **2016**, *351* (6273), 579-582. DOI: doi:10.1126/science.aad2212.

(8) Macfarlane, R. J.; Jones, M. R.; Lee, B.; Auyeung, E.; Mirkin, C. A. Topotactic Interconversion of Nanoparticle Superlattices. *Science* **2013**, *341* (6151), 1222-1225. DOI: doi:10.1126/science.1241402.

(9) Mason, J. A.; Laramy, C. R.; Lai, C.-T.; O'Brien, M. N.; Lin, Q.-Y.; Dravid, V. P.; Schatz, G. C.; Mirkin, C. A. Contraction and Expansion of Stimuli-Responsive DNA Bonds in Flexible Colloidal Crystals. *Journal of the American Chemical Society* **2016**, *138* (28), 8722-8725. DOI: 10.1021/jacs.6b05430.

(10) Samanta, D.; Iscen, A.; Laramy, C. R.; Ebrahimi, S. B.; Bujold, K. E.; Schatz, G. C.; Mirkin, C. A. Multivalent Cation-Induced Actuation of DNA-Mediated Colloidal Superlattices. *Journal of the American Chemical Society* **2019**, *141* (51), 19973-19977. DOI: 10.1021/jacs.9b09900.

(11) Xiong, Q.; Lee, O.-S.; Mirkin, C. A.; Schatz, G. Ethanol-Induced Condensation and Decondensation in DNA-Linked Nanoparticles: A Nucleosome-like Model for the Condensed State. *Journal of the American Chemical Society* **2023**, *145* (1), 706-716. DOI: 10.1021/jacs.2c11834.

(12) Young, K. L.; Ross, M. B.; Blaber, M. G.; Rycenga, M.; Jones, M. R.; Zhang, C.; Senesi, A. J.; Lee, B.; Schatz, G. C.; Mirkin, C. A. Using DNA to Design Plasmonic Metamaterials with Tunable Optical Properties. *Advanced Materials* **2014**, *26* (4), 653-659. DOI: https://doi.org/10.1002/adma.201302938.

(13) Auyeung, E.; Morris, W.; Mondloch, J. E.; Hupp, J. T.; Farha, O. K.; Mirkin, C. A. Controlling Structure and Porosity in Catalytic Nanoparticle Superlattices with DNA. *Journal of the American Chemical Society* **2015**, *137* (4), 1658-1662. DOI: 10.1021/ja512116p.

(14) Ross, M. B.; Ku, J. C.; Vaccarezza, V. M.; Schatz, G. C.; Mirkin, C. A. Nanoscale form dictates mesoscale function in plasmonic DNA–nanoparticle superlattices. *Nature Nanotechnology* **2015**, *10* (5), 453-458. DOI: 10.1038/nnano.2015.68.

(15) Kim, S.; Zheng, C. Y.; Schatz, G. C.; Aydin, K.; Kim, K.-H.; Mirkin, C. A. Mie-Resonant Three-Dimensional Metacrystals. *Nano Letters* **2020**, *20* (11), 8096-8101. DOI: 10.1021/acs.nanolett.0c03089.

(16) Li, Y.; Jin, H.; Zhou, W.; Wang, Z.; Lin, Z.; Mirkin, C. A.; Espinosa, H. D. Ultrastrong colloidal crystal metamaterials engineered with DNA. *Science Advances* **2023**, *9* (39), eadj8103. DOI: doi:10.1126/sciadv.adj8103.

(17) Seo, S. E.; Girard, M.; Olvera de la Cruz, M.; Mirkin, C. A. Non-equilibrium anisotropic colloidal single crystal growth with DNA. *Nature Communications* **2018**, *9* (1), 4558. DOI: 10.1038/s41467-018-06982-9.

(18) Lewis, D. J.; Zornberg, L. Z.; Carter, D. J. D.; Macfarlane, R. J. Single-crystal Winterbottom constructions of nanoparticle superlattices. *Nature Materials* **2020**, *19* (7), 719-724. DOI: 10.1038/s41563-020-0643-6.

(19) Auyeung, E.; Li, T. I. N. G.; Senesi, A. J.; Schmucker, A. L.; Pals, B. C.; de la Cruz, M. O.; Mirkin, C. A. DNA-mediated nanoparticle crystallization into Wulff polyhedra. *Nature* **2014**, *505* (7481), 73-77. DOI: 10.1038/nature12739.

(20) Calcaterra, H. A.; Chellam, N. S.; Lee, B.; Schatz, G. C.; Mirkin, C. A. High Temperature, Isothermal Growth Promotes Close Packing and Thermal Stability in DNA-Engineered Colloidal Crystals. *ACS Nano* **2024**, *18* (41), 28268-28278. DOI: 10.1021/acsnano.4c09308.

(21) Park, S.-J.; Lazarides, A. A.; Storhoff, J. J.; Pesce, L.; Mirkin, C. A. The Structural Characterization of Oligonucleotide-Modified Gold Nanoparticle Networks Formed by DNA Hybridization. *The Journal of Physical Chemistry B* **2004**, *108* (33), 12375-12380. DOI: 10.1021/jp040242b.

(22) Biancaniello, P. L.; Kim, A. J.; Crocker, J. C. Colloidal Interactions and Self-Assembly Using DNA Hybridization. *Physical Review Letters* **2005**, *94* (5), 058302. DOI: 10.1103/PhysRevLett.94.058302.

(23) Hill, H. D.; Macfarlane, R. J.; Senesi, A. J.; Lee, B.; Park, S. Y.; Mirkin, C. A. Controlling the Lattice Parameters of Gold Nanoparticle FCC Crystals with Duplex DNA Linkers. *Nano Letters* **2008**, *8* (8), 2341-2344. DOI: 10.1021/nl8011787.

(24) Lee, O.-S.; Schatz, G. C. Molecular Dynamics Simulation of DNA-Functionalized Gold Nanoparticles. *The Journal of Physical Chemistry C* **2009**, *113* (6), 2316-2321. DOI: 10.1021/jp8094165.

(25) Wang, Y.; Wang, Y.; Zheng, X.; Ducrot, É.; Yodh, J. S.; Weck, M.; Pine, D. J. Crystallization of DNA-coated colloids. *Nature Communications* **2015**, *6* (1), 7253. DOI: 10.1038/ncomms8253.

(26) Tian, Y.; Zhang, Y.; Wang, T.; Xin, H. L.; Li, H.; Gang, O. Lattice engineering through nanoparticle–DNA frameworks. *Nature Materials* **2016**, *15* (6), 654-661. DOI: 10.1038/nmat4571.

(27) Rogers, W. B.; Shih, W. M.; Manoharan, V. N. Using DNA to program the self-assembly of colloidal nanoparticles and microparticles. *Nature Reviews Materials* **2016**, *1* (3), 16008. DOI: 10.1038/natrevmats.2016.8.

(28) Howie, A.; Marks, L. D. Elastic strains and the energy balance for multiply twinned particles. *Philosophical Magazine A* **1984**, *49* (1), 95-109. DOI: 10.1080/01418618408233432.

(29) Rupich, S. M.; Shevchenko, E. V.; Bodnarchuk, M. I.; Lee, B.; Talapin, D. V. Size-Dependent Multiple Twinning in Nanocrystal Superlattices. *Journal of the American Chemical Society* **2010**, *132* (1), 289-296. DOI: 10.1021/ja9074425.

(30) Lee, S.-J.; Kim, J.; Dey, J.; Jin, K. S.; Choi, S.-M. Nanoparticle Superlattices Driven by Linker-Mediated Covalent Bonding Interaction. *The Journal of Physical Chemistry Letters* **2024**, *15* (25), 6691-6698. DOI: 10.1021/acs.jpclett.4c01469.

(31) Compton, O. C.; Osterloh, F. E. Evolution of Size and Shape in the Colloidal Crystallization of Gold Nanoparticles. *Journal of the American Chemical Society* **2007**, *129* (25), 7793-7798. DOI: 10.1021/ja069033q.

(32) Woodcock, L. V. Entropy difference between the face-centred cubic and hexagonal close-packed crystal structures. *Nature* **1997**, *385* (6612), 141-143. DOI: 10.1038/385141a0.

(33) El-Danaf, E.; Kalidindi, S. R.; Doherty, R. D. Influence of grain size and stacking-fault energy on deformation twinning in fcc metals. *Metallurgical and Materials Transactions A* **1999**, *30* (5), 1223-1233. DOI: 10.1007/s11661-999-0272-9.

(34) Byelov, D. V.; Hilhorst, J.; Leferink op Reinink, A. B. G. M.; Snigireva, I.; Snigirev, A.; Vaughan, G. B. M.; Portale, G.; Petukhov, A. V. Diffuse scattering in random-stacking hexagonal close-packed crystals of colloidal hard spheres. *Phase Transitions* **2010**, *83* (2), 107-114. DOI: 10.1080/01411590903586452.

(35) Ma, T.; Kapustin, E. A.; Yin, S. X.; Liang, L.; Zhou, Z.; Niu, J.; Li, L.-H.; Wang, Y.; Su, J.; Li, J.; et al. Single-crystal x-ray diffraction structures of covalent organic frameworks. *Science* **2018**, *361* (6397), 48-52. DOI: 10.1126/science.aat7679 (acccessed 2024/11/11).

(36) Zhang, Z.; Song, J.; Besenbacher, F.; Dong, M.; Gothelf, K. V. Self-Assembly of DNA Origami and Single-Stranded Tile Structures at Room Temperature. *Angewandte Chemie International Edition* **2013**, *52* (35), 9219-9223. DOI: https://doi.org/10.1002/anie.201303611 (acccessed 2024/11/11).

(37) Jungmann, R.; Liedl, T.; Sobey, T. L.; Shih, W.; Simmel, F. C. Isothermal Assembly of DNA Origami Structures Using Denaturing Agents. *Journal of the American Chemical Society* **2008**, *130* (31), 10062-10063. DOI: 10.1021/ja8030196.

(38) Högberg, B.; Liedl, T.; Shih, W. M. Folding DNA Origami from a Double-Stranded Source of Scaffold. *Journal of the American Chemical Society* **2009**, *131* (26), 9154-9155. DOI: 10.1021/ja902569x.

(39) Kim, J.; Lee, S.-J.; Dey, J.; Jang, J.; Kim, Y. Y.; Choi, S.-M. Size Tunable Synthesis of Covalently Linked Nanoparticle Superlattices via Temperature Control. *The Journal of Physical Chemistry C* **2024**, *128* (28), 11960-11965. DOI: 10.1021/acs.jpcc.4c03372.

(40) Dey, J.; Lee, S.-J.; Kim, J.; Lim, S.-H.; Ha, J.-M.; Lee, M.-J.; Choi, S.-M. Spontaneous Formation of Highly Stable Nanoparticle Supercrystals Driven by a Covalent Bonding Interaction. *Nano Letters* **2021**, *21* (1), 258-264. DOI: 10.1021/acs.nanolett.0c03616.

(41) Ringe, E.; Van Duyne, R. P.; Marks, L. D. Kinetic and Thermodynamic Modified Wulff Constructions for Twinned Nanoparticles. *The Journal of Physical Chemistry C* **2013**, *117* (31), 15859-15870. DOI: 10.1021/jp401566m.

(42) Sun, M.; Cheng, Z.; Chen, W.; Jones, M. Understanding Symmetry Breaking at the Single-Particle Level via the Growth of Tetrahedron-Shaped Nanocrystals from Higher-Symmetry Precursors. *ACS Nano* **2021**, *15* (10), 15953-15961. DOI: 10.1021/acsnano.1c04056.

(43) Xia, Y.; Xia, X.; Peng, H.-C. Shape-Controlled Synthesis of Colloidal Metal Nanocrystals: Thermodynamic versus Kinetic Products. *Journal of the American Chemical Society* **2015**, *137* (25), 7947-7966. DOI: 10.1021/jacs.5b04641.

(44) Tsao, J. Y. Chapter 6 - Surface Morphology. In *Materials Fundamentals of Molecular Beam Epitaxy*, Tsao, J. Y. Ed.; Academic Press, 1993; pp 201-257.

(45) Ramana Murty, M. V.; Cooper, B. H. Influence of step edge diffusion on surface morphology during epitaxy. *Surface Science* **2003**, *539* (1), 91-98. DOI: https://doi.org/10.1016/S0039-6028(03)00749-0.

(46) Jeong, H.-C.; Williams, E. D. Steps on surfaces: experiment and theory. *Surface Science Reports* **1999**, *34* (6), 171-294. DOI: https://doi.org/10.1016/S0167-5729(98)00010-7.

(47) Calcaterra, H. A.; Zheng, C. Y.; Seifert, S.; Yao, Y.; Jiang, Y.; Mirkin, C. A.; Deng, J.; Lee, B. Hints of Growth Mechanism Left in Supercrystals. *ACS Nano* **2023**, *17* (16), 15999-16007. DOI: 10.1021/acsnano.3c04365.

(48) Rode, D. L. Crystal growth terraces and surface reconstruction. *Journal of Crystal Growth* **1974**, *27*, 313-315. DOI: https://doi.org/10.1016/S0022-0248(74)80079-5.

(49) Analysis of Thermal Melting Curves. *Oligonucleotides* **2003**, *13* (6), 515-537. DOI: 10.1089/154545703322860825.

(50) Vologodskii, A.; Frank-Kamenetskii, M. D. DNA melting and energetics of the double helix. *Physics of Life Reviews* **2018**, *25*, 1-21. DOI: https://doi.org/10.1016/j.plrev.2017.11.012.

(51) Blake, R. D.; Delcourt, S. G. Thermodynamic Effects of Formamide on DNA Stability. *Nucleic Acids Research* **1996**, *24* (11), 2095-2103. DOI: 10.1093/nar/24.11.2095 (acccessed 1/9/2024).

(52) Hammouda, B.; Worcester, D. The Denaturation Transition of DNA in Mixed Solvents. *Biophysical Journal* **2006**, *91* (6), 2237-2242. DOI: https://doi.org/10.1529/biophysj.106.083691.

(53) Hoff, A. J.; Roos, A. L. M. Hysteresis of denaturation of DNA in the melting range. *Biopolymers* **1972**, *11* (6), 1289-1294. DOI: https://doi.org/10.1002/bip.1972.360110612.

(54) Shim, A. R.; Frederick, J.; Pujadas, E. M.; Kuo, T.; Ye, I. C.; Pritchard, J. A.; Dunton, C. L.; Gonzalez, P. C.; Acosta, N.; Jain, S.; et al. Formamide denaturation of double-stranded DNA for fluorescence in situ hybridization (FISH) distorts nanoscale chromatin structure. *PLOS ONE* **2024**, *19* (5), e0301000. DOI: 10.1371/journal.pone.0301000.

(55) O'Brien, M. N.; Jones, M. R.; Brown, K. A.; Mirkin, C. A. Universal Noble Metal Nanoparticle Seeds Realized Through Iterative Reductive Growth and Oxidative Dissolution Reactions. *Journal of the American Chemical Society* **2014**, *136* (21), 7603-7606. DOI: 10.1021/ja503509k.

(56) Zheng, Y.; Zeng, J.; Ruditskiy, A.; Liu, M.; Xia, Y. Oxidative Etching and Its Role in Manipulating the Nucleation and Growth of Noble-Metal Nanocrystals. *Chemistry of Materials* **2014**, *26* (1), 22-33. DOI: 10.1021/cm402023g.

(57) Umemura, A.; Diring, S.; Furukawa, S.; Uehara, H.; Tsuruoka, T.; Kitagawa, S. Morphology Design of Porous Coordination Polymer Crystals by Coordination Modulation. *Journal of the American Chemical Society* **2011**, *133* (39), 15506-15513. DOI: 10.1021/ja204233q.

(58) Bian, T.; Gardin, A.; Gemen, J.; Houben, L.; Perego, C.; Lee, B.; Elad, N.; Chu, Z.; Pavan, G. M.; Klajn, R. Electrostatic co-assembly of nanoparticles with oppositely charged small molecules into static and dynamic superstructures. *Nature Chemistry* **2021**, *13* (10), 940-949. DOI: 10.1038/s41557-021-00752-9.

(59) Wang, X.; Wu, L.; Wang, G.; Chen, G. Dynamic Crystallization and Phase Transition in Evaporating Colloidal Droplets. *Nano Letters* **2019**, *19* (11), 8225-8233. DOI: 10.1021/acs.nanolett.9b03633.

(60) Jin, R.; Wu, G.; Li, Z.; Mirkin, C. A.; Schatz, G. C. What Controls the Melting Properties of DNA-Linked Gold Nanoparticle Assemblies? *Journal of the American Chemical Society* **2003**, *125* (6), 1643-1654. DOI: 10.1021/ja021096v.

(61) Eberle, A. P. R.; Castañeda-Priego, R.; Kim, J. M.; Wagner, N. J. Dynamical Arrest, Percolation, Gelation, and Glass Formation in Model Nanoparticle Dispersions with Thermoreversible Adhesive Interactions. *Langmuir* **2012**, *28* (3), 1866-1878. DOI: 10.1021/la2035054.

(62) Berryman, J. G. Random close packing of hard spheres and disks. *Physical Review A* **1983**, *27* (2), 1053-1061. DOI: 10.1103/PhysRevA.27.1053.

(63) Haxton, T. K.; Hedges, L. O.; Whitelam, S. Crystallization and arrest mechanisms of model colloids. *Soft Matter* **2015**, *11* (48), 9307-9320, 10.1039/C5SM01833A. DOI: 10.1039/C5SM01833A.

(64) Hagan, M. F.; Chakraborty, A. K. Hybridization dynamics of surface immobilized DNA. *The Journal of Chemical Physics* **2004**, *120* (10), 4958-4968. DOI: 10.1063/1.1645786 (acccessed 11/12/2024).

(65) de Gennes, P. G. Conformations of Polymers Attached to an Interface. *Macromolecules* **1980**, *13* (5), 1069-1075. DOI: 10.1021/ma60077a009.

(66) Lytton-Jean, A. K. R.; Mirkin, C. A. A Thermodynamic Investigation into the Binding Properties of DNA Functionalized Gold Nanoparticle Probes and Molecular Fluorophore Probes. *Journal of the American Chemical Society* **2005**, *127* (37), 12754-12755. DOI: 10.1021/ja052255o.

(67) Hurst, S. J.; Lytton-Jean, A. K.; Mirkin, C. A. Maximizing DNA loading on a range of gold nanoparticle sizes. *Analytical chemistry* **2006**, *78* (24), 8313-8318.

(68) Harp, J. M.; Coates, L.; Sullivan, B.; Egli, M. Water structure around a left-handed Z-DNA fragment analyzed by cryo neutron crystallography. *Nucleic Acids Research* **2021**, *49* (8), 4782-4792. DOI: 10.1093/nar/gkab264 (acccessed 1/8/2024).

(69) Likhtenshtein, G. I. Nucleic Acids Hydration. In *Biological Water: Physicochemical Aspects*, Likhtenshtein, G. I. Ed.; Springer International Publishing, 2021; pp 371-405.

(70) Eichinger, B. K.; Fixman, M. Helix–coil transition in heterogeneous chains. II. DNA model. *Biopolymers* **1970**, *9* (2), 205-221. DOI: https://doi.org/10.1002/bip.1970.360090206 (acccessed 2024/01/08).

(71) Pauw, B. R. Everything SAXS: small-angle scattering pattern collection and correction. *Journal of Physics: Condensed Matter* **2013**, *25* (38), 383201. DOI: 10.1088/0953-8984/25/38/383201.

(72) Senesi, A. J.; Lee, B. Small-angle scattering of particle assemblies. *Journal of Applied Crystallography* **2015**, *48* (4), 1172-1182. DOI: https://doi.org/10.1107/S1600576715011474.

(73) Scherrer, P. Bestimmung der inneren Struktur und der Größe von Kolloidteilchen mittels Röntgenstrahlen. In *Kolloidchemie Ein Lehrbuch*, Zsigmondy, R. Ed.; Springer Berlin Heidelberg, 1912; pp 387-409.

(74) Jack, R. L.; Hagan, M. F.; Chandler, D. Fluctuation-dissipation ratios in the dynamics of self-assembly. *Physical Review E* **2007**, *76* (2), 021119. DOI: 10.1103/PhysRevE.76.021119.

(75) Klotsa, D.; Jack, R. L. Predicting the self-assembly of a model colloidal crystal. *Soft Matter* **2011**, *7* (13), 6294-6303, 10.1039/C1SM05456B. DOI: 10.1039/C1SM05456B.

(76) Tanner, C. P. N.; Utterback, J. K.; Portner, J.; Coropceanu, I.; Das, A.; Tassone, C. J.; Teitelbaum, S. W.; Limmer, D. T.; Talapin, D. V.; Ginsberg, N. S. In Situ X-ray Scattering Reveals Coarsening Rates of Superlattices Self-Assembled from Electrostatically Stabilized Metal Nanocrystals Depend Nonmonotonically on Driving Force. *ACS Nano* **2024**, *18* (7), 5778-5789. DOI: 10.1021/acsnano.3c12186.

(77) Coropceanu, I.; Janke, E. M.; Portner, J.; Haubold, D.; Nguyen, T. D.; Das, A.; Tanner, C. P. N.; Utterback, J. K.; Teitelbaum, S. W.; Hudson, M. H.; et al. Self-assembly of nanocrystals into strongly electronically coupled all-inorganic supercrystals. *Science* **2022**, *375* (6587), 1422-1426. DOI: doi:10.1126/science.abm6753.

(78) Hueckel, T.; Woo, S.; Macfarlane, R. J. Controlling the thermally-driven crystallization of DNA-coated nanoparticles with formamide. *Soft Matter* **2024**, *20* (34), 6723-6729, 10.1039/D4SM00854E. DOI: 10.1039/D4SM00854E.

(79) Seo, S. E.; Wang, M. X.; Shade, C. M.; Rouge, J. L.; Brown, K. A.; Mirkin, C. A. Modulating the Bond Strength of DNA–Nanoparticle Superlattices. *ACS Nano* **2016**, *10* (2), 1771-1779. DOI: 10.1021/acsnano.5b07103.

(80) Lee, S.; Zheng, C. Y.; Bujold, K. E.; Mirkin, C. A. A Cross-Linking Approach to Stabilizing Stimuli-Responsive Colloidal Crystals Engineered with DNA. *Journal of the American Chemical Society* **2019**, *141* (30), 11827-11831. DOI: 10.1021/jacs.9b06106.

(81) Pal, S.; Zhang, Y.; Kumar, S. K.; Gang, O. Dynamic Tuning of DNA-Nanoparticle Superlattices by Molecular Intercalation of Double Helix. *Journal of the American Chemical Society* **2015**, *137* (12), 4030-4033. DOI: 10.1021/ja512799d.

(82) Oh, T.; Park, S. S.; Mirkin, C. A. Stabilization of Colloidal Crystals Engineered with DNA. *Advanced Materials* **2019**, *31* (1), 1805480. DOI: https://doi.org/10.1002/adma.201805480.

(83) Senesi, A.; Lee, B. Scattering functions of polyhedra. *Journal of Applied Crystallography* **2015**, *48* (2), 565-577. DOI: doi:10.1107/S1600576715002964.

(84) Scardi, P.; Leoni, M.; Delhez, R. Line broadening analysis using integral breadth methods: a critical review. *Journal of Applied Crystallography* **2004**, *37* (3), 381-390. DOI: doi:10.1107/S0021889804004583.

(85) Ilavsky, J.; Jemian, P. R. Irena: tool suite for modeling and analysis of small-angle scattering. *Journal of Applied Crystallography* **2009**, *42* (2), 347-353. DOI: doi:10.1107/S0021889809002222.

(86) Li, S.; Olson, W. K.; Lu, X.-J. Web 3DNA 2.0 for the analysis, visualization, and modeling of 3D nucleic acid structures. *Nucleic Acids Res.* **2019**, *47* (W1), W26-W34.

(87) Hanwell, M. D.; Curtis, D. E.; Lonie, D. C.; Vandermeersch, T.; Zurek, E.; Hutchison, G. R. Avogadro: an advanced semantic chemical editor, visualization, and analysis platform. *Journal of cheminformatics* **2012**, *4* (1), 1-17.

(88) Heinz, H.; Vaia, R.; Farmer, B.; Naik, R. Accurate simulation of surfaces and interfaces of face-centered cubic metals using 12− 6 and 9− 6 Lennard-Jones potentials. *J. Phys. Chem. C* **2008**, *112* (44), 17281-17290.

(89) Hart, K.; Foloppe, N.; Baker, C. M.; Denning, E. J.; Nilsson, L.; MacKerell Jr, A. D. Optimization of the CHARMM additive force field for DNA: Improved treatment of the BI/BII conformational equilibrium. *J. Chem. Theory Comput.* **2012**, *8* (1), 348-362.

(90) Vanommeslaeghe, K.; Hatcher, E.; Acharya, C.; Kundu, S.; Zhong, S.; Shim, J.; Darian, E.; Guvench, O.; Lopes, P.; Vorobyov, I. CHARMM general force field: A force field for drug-like molecules compatible with the CHARMM all-atom additive biological force fields. *J. Comput. Chem.* **2010**, *31* (4), 671-690.

(91) Phillips, J. C.; Braun, R.; Wang, W.; Gumbart, J.; Tajkhorshid, E.; Villa, E.; Chipot, C.; Skeel, R. D.; Kale, L.; Schulten, K. Scalable molecular dynamics with NAMD. *J. Comput. Chem.* **2005**, *26* (16), 1781-1802.

(92) Feller, S. E.; Zhang, Y.; Pastor, R. W.; Brooks, B. R. Constant pressure molecular dynamics simulation: The Langevin piston method. *J. Chem. Phys.* **1995**, *103* (11), 4613-4621.

(93) Martyna, G. J.; Tobias, D. J.; Klein, M. L. Constant pressure molecular dynamics algorithms. *J. Chem. Phys.* **1994**, *101* (5), 4177-4189.

(94) Darden, T.; York, D.; Pedersen, L. Particle mesh Ewald: An N· log (N) method for Ewald sums in large systems. *The Journal of chemical physics* **1993**, *98* (12), 10089-10092.